

State-selective electron capture following Ar^{8+} –Li collisions for impact energies from 0.1 to 1.0 keV amu^{−1}

C Laulhé[†], E Jacquet^{†‡}, P Boduch^{†‡}, M Chantepie^{†‡}, N Gherardi[†],
X Husson^{†‡}, D Lecler[†] and J Pascale[§]

[†] Laboratoire de spectroscopie atomique, ISMRA, 6 boulevard Maréchal Juin, F-14050, Caen Cedex, France

[‡] UFR des Sciences, Université de Caen-Basse Normandie, Esplanade de la Paix, F-14032, Caen Cedex, France

[§] Service des Photons, Atomes et Molécules, Centre d'Etudes de Saclay, CEA, Bâtiment 522, F-91191, Gif sur Yvette Cedex, France

Received 8 November 1996, in final form 27 February 1997

Abstract. The effect of the velocity of the incident ions in the $n\ell$ -distributions for $n = 8$ and 9 of the electron capture in collisions of highly charged Ar^{8+} ions with a lithium target is studied in the 0.1–1 keV amu^{−1} energy range. The experimental $n\ell$ -distributions are deduced from the measured emission cross sections of all lines corresponding to $7\ell' - 8\ell$ and $8\ell' - 9\ell$ transitions. The results of theoretical calculations using the three-body classical trajectory Monte Carlo (CTMC) method are presented for the Ar^{8+} –Li(2s) system and also for the O^{8+} –Li(2s) system in order to show the influence of the Ar^{8+} core electrons on the final $n\ell$ -distributions. The experimental and theoretical results are found to be in fair agreement except for the 9s and 9p cross sections. The presence of the projectile core electrons strongly affects the population and the collision energy dependence of low- ℓ values produced in the electron capture reaction. In particular, the $\sigma(n\ell)$ partial cross sections ($n = 8, 9$ and $\ell = 0, 1, 2$) increase with decreasing energies and go through a maximum for $\sigma(8s)$ and $\sigma(8p)$. Electronic energy curve calculations for the $(\text{Ar}^{7+} + \text{Li})^+$ and $(\text{O}^{7+} + \text{Li})^+$ systems allow us to discuss the results in terms of dynamical couplings.

Introduction

Collisions at intermediate velocities of multiply charged ions on lithium atoms are of special interest for fusion plasma diagnostics (Schorn *et al* 1991, Brazuk *et al* 1985), especially to determine both the densities and temperatures of plasma impurities without the need for a complicated and ambiguous plasma modelling procedure. Wolfrum *et al* (1992), Hoekstra *et al* (1993) and Rieger *et al* (1995) studied collisions on Li atoms experimentally by means of visible photon spectroscopy. In the case of an X^{6+} ($\text{X} \equiv \text{C}, \text{N}, \text{O}$ and Ne) projectile, they measured total cross sections for $n = 7 \rightarrow 6$ and $n = 8 \rightarrow 7$ transitions and they found that the core effects are negligible to first order. In the case of B^{5+} and N^{5+} –Li collisions, a similar result was found. Schweinzer *et al* (1994) calculated total single-electron capture cross sections in collisions of fully stripped ions with Li(2s) atoms by using an atomic-orbital close-coupling method. They derived a scaling formula with respect to the initial binding energy of the electron in the target and the charge of the ion, which gives a reduced cross section versus a reduced projectile energy in the range 1–80 keV amu^{−1}. This scaling formula agrees well with all experimental and theoretical

data, except for $H^+Li(2s)$ collisions in the energy range below 20 keV amu^{-1} . In particular, the scaling formula predicts a reduced total cross section which is almost energy independent for reduced energies between 1 and 10 keV amu^{-1} . This latter result is explained by the availability of electron capture channels within the reaction window at all energies.

The choice of Ar^{8+} as the projectile allowed us to deduce $\sigma(n\ell)$ cross sections ($n = 8$ and 9) from emission line cross sections. Collisions between Ar^{8+} ions and Li atoms have already been studied experimentally for impact energies from 1.5 to 4.5 keV amu^{-1} by means of near-UV and visible photon spectroscopy. Three-body classical trajectory Monte Carlo (CTMC) calculations for these collisions were performed for impact energies from 1.0 – 4.0 keV amu^{-1} (Jacquet *et al* 1995). The experimental $\sigma(n\ell)$ cross sections for capture into the $n\ell$ sublevels of Ar^{7+} ions produced by single-electron capture were found to be, for the most populated $n = 8$ and 9 levels, in fair agreement with the CTMC results. These final $n\ell$ distributions are not statistical: states with large ℓ values are strongly populated, but also states with low- ℓ values ($\ell = 0, 1, 2$). This result was attributed to a core-electron effect, as already predicted by CTMC calculations for N^{5+} and $Ar^{8+}Cs(6s)$ collisions (Pascale *et al* 1990). The final $n\ell$ distributions depend strongly on the projectile energy as already predicted by CTMC calculations (Jacquet *et al* 1994). Indeed, the populations of the states of large angular momenta do not depend on the projectile energies in the studied energy range, but, for a given n state ($n = 8, 9$ and $\ell = 0, 1, 2$), the $\sigma(n\ell)$ cross sections increase more or less strongly with decreasing energies showing that the effect of the projectile core electrons is strongly energy dependent.

In the case of $Kr^{8+}Li$ collisions, the $\sigma(8s)$ cross section goes through a maximum when the projectile energy decreases, whereas the $\sigma(n\ell)$ cross sections for the largest values of ℓ decrease (Jacquet *et al* 1994). For $Ar^{8+}Li$ collisions, it should be the same but the maximum of the $\sigma(8s)$ cross section should occur at a lower energy than in the case of $Kr^{8+}Li$ collisions since the energy splitting at the avoided crossing responsible for electron capture into the $8s$ final sublevel is larger for Kr^{8+} than for Ar^{8+} (Jacquet *et al* 1994). The $Ar^{8+}Li(2s)$ collisions were then studied experimentally for incident energies between 0.1 and 1.0 keV amu^{-1} . Three-body classical trajectory Monte Carlo (CTMC) calculations (Abrines and Percival 1966, Olson and Salop 1977) were also performed for the same energy range. Though the classical approach is well adapted to the study of electron capture into high excited levels, it is interesting to test its ability to predict state-selective cross sections in the low-energy range investigated here, where the *quasi-molecular* collision regime is reached. In order to show more clearly the Ar^{8+} core-electron effect on the final $n\ell$ -distributions, CTMC calculations were also performed for $O^{8+}Li(2s)$ collisions at a few energies.

In this paper we report experimental results on the energy dependence of the projectile core-electron effect on the final 8ℓ - and 9ℓ -distributions in $Ar^{8+}Li(2s)$ collisions along with our CTMC calculations for O^{8+} and $Ar^{8+}Li(2s)$ collisions. The experimental set-up and a spectroscopic analysis will be presented, in particular, the ion beam decelerating device which was constructed for these experiments will be described.

1. Experimental set-up

The incident Ar^{8+} ions were extracted from an ECR source of the GANIL[†] test bench with a potential of $U_0 = 12.5 \text{ kV}$. The incident beam was focused on an effusive jet of lithium

[†] Grand Accélérateur National d'Ions Lourds, Caen, France.

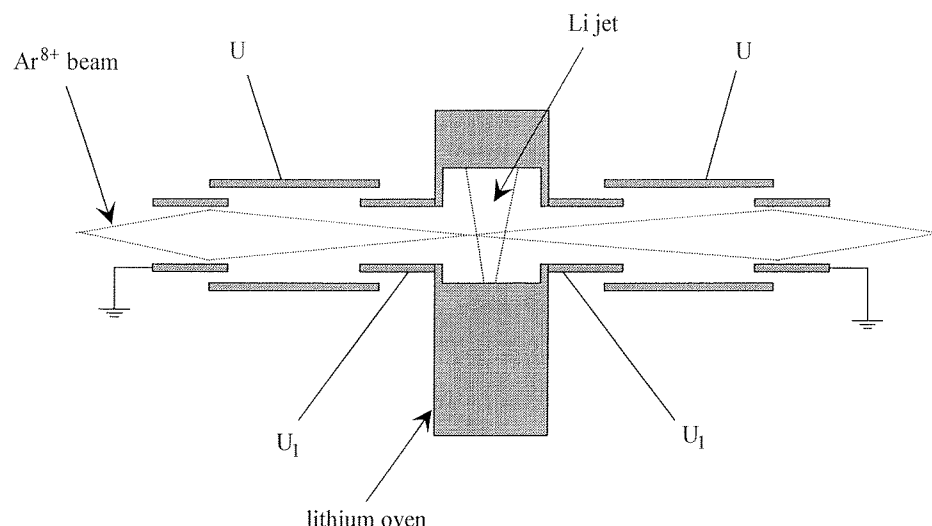


Figure 1. Ion beam decelerating device used to study Ar^{8+} -Li(2s) collisions for energies between 0.1 and 1.0 keV amu⁻¹.

atoms inside the collision chamber. Solid lithium was evaporated in an oven which was heated up with a thermocoaxial cable; in order to avoid heating of the walls of the collision chamber, the furnace was placed in a lining which was cooled by water circulation. The ion beam decelerating device was placed in the middle of the collision chamber.

The ion beam decelerating device is presented in figure 1. It was composed of two electrostatic lens systems. The first one was situated just in front of the Li jet and was at a potential $U_1 < U_0$. The ion beam was then decelerated to an energy of $(U_0 - U_1)q$ eV in the collision area (i.e. in the Li jet). Since the ion beam line was at the ground of the ion source, it was necessary to accelerate the ions after the collision area in order to collect them in a Faraday cup and measure the ion beam intensity. The second electrostatic lens was then placed after the Li jet and was at a potential U_1 . The ion beam then had an energy of U_0q keV after the decelerating device. The ion beam was likely to diverge inside the interaction zone, due to a strong space-charge effect, so a third electrode was added. This electrode was at an intermediate potential U , adjusted to focus the ion beam on the collision area (just above the lithium oven). The potential in the collision area was rather homogeneous (for example, $U_1 - U_0 = 500 \pm 3$ V). 95% of the ion beam produced by the ion source was collected in the Faraday cup for the lower energy used in these experiments (500q eV). The value of the extraction potential U_0 (12.5 kV) of the ECR ion source was chosen so that a strong and stable ion current was provided (the ion beam intensity was about 100 μA). The extraction potential U_0 was measured precisely and consequently the potential U_1 was fixed.

The emitted photons were observed at right angles to the directions of the incident ion beam and of the Li jet. They were analysed with a normal-incident grating spectrometer of 700 mm focal length which contains a 1200 grooves/mm grating blazed for 750 nm in the first order. They were detected in the 200–600 nm wavelength range with a photomultiplier (Hamamatsu R106). The spectral analyses of such emissions have already been presented in detail (Jacquet *et al* 1993). However, a few new lines were observed in the spectra recorded at very low incident energies (0.1 and 0.2 keV amu⁻¹).

In order to determine emission cross sections for each single-electron capture line, we have recorded the spectrum corresponding to Ar^{8+} –Li collisions at 1.5 keV amu^{-1} . The emission cross sections for this energy have already been determined (Jacquet *et al* 1995), the cross sections for collision energies between 0.1 and 1.0 keV amu^{-1} were deduced from ones for 1.5 keV amu^{-1} Ar^{8+} –Li collisions.

2. Spectroscopic results

In the spectra corresponding to very low incident energies (0.1 and 0.2 keV amu^{-1}), a few new lines were observed. These new lines are presented in table 1. They were identified using experimental data already obtained by Boduch *et al* (1992) and theoretical data obtained from spectroscopic *ab initio* pseudo-relativistic Hartree–Fock (HFR) calculations using the Cowan code (1981). In the spectroscopic analysis of Ar^{8+} – H_2 collisions, Boduch *et al* (1992) observed lines corresponding to the various components of $5s$ – $5p$ and $5p$ – $5d$ transitions; these five lines were also observed in the spectra resulting from the present low-energy Ar^{8+} –Li collisions. HFR calculations allowed us to identify the lines corresponding to the $8s$ – $9p$ and $8d$ – $9p$ transitions. Fine-structure splittings of the $5p$ 2P , $5d$ 2D , $8d$ 2D and $9p$ 2P terms (table 2) were deduced from the present identifications. They are in good agreement with both experimental data from Boduch *et al* (1992) and theoretical HFR calculations.

The two lines corresponding to $6g$ – $7h$ and $6h$ – $7i$ transitions are indicated in table 1. These two lines have already been observed in the spectra resulting from Ar^{8+} –Li(2s) collisions but are not clearly identified. The emission cross sections of these two lines cannot be evaluated because the spectroscopic response of the optical device is not known

Table 1. Experimental and predicted wavelengths of transitions in Ar VIII observed in Ar^{8+} –Li collisions. (1) HFR calculations; (2) experimental data from Boduch *et al* (1992); (3) this experiment.

Transition in Ar VIII	λ_{calc} (nm) in vacuum (1)	λ_{exp} (nm) in air (2)	λ_{exp} (nm) in air (3)
$5s \ ^2S_{1/2}$ – $5p \ ^2P_{1/2}$	398.64	400.23 ± 0.04	400.30 ± 0.04
$5s \ ^2S_{1/2}$ – $5p \ ^2P_{3/2}$	391.61	392.69 ± 0.04	392.71 ± 0.04
$5p \ ^2P_{1/2}$ – $5d \ ^2D_{3/2}$	303.83	302.83 ± 0.03	302.81 ± 0.04
$5p \ ^2P_{3/2}$ – $5d \ ^2D_{3/2}$	308.05	307.34 ± 0.03	307.32 ± 0.04
$5p \ ^2P_{3/2}$ – $5d \ ^2D_{5/2}$	307.54	306.94 ± 0.03	306.93 ± 0.04
$8s \ ^2S_{1/2}$ – $9p \ ^2P_{1/2}$	316.12		316.18 ± 0.04
$8s \ ^2S_{1/2}$ – $9p \ ^2P_{3/2}$	315.42		315.41 ± 0.04
$8d \ ^2D_{3/2}$ – $9p \ ^2P_{1/2}$	534.07		534.22 ± 0.04
$8d \ ^2D_{3/2}$ – $9p \ ^2P_{3/2}$	532.07		532.10 ± 0.04
$8d \ ^2D_{5/2}$ – $9p \ ^2P_{3/2}$	532.44		532.40 ± 0.04
$6g \ ^2G_{7/2}$ – $7h \ ^2H_{9/2}$	192.55		
$6g \ ^2G_{9/2}$ – $7h \ ^2H_{9/2}$	192.57		192.94 ± 0.02
$6g \ ^2G_{9/2}$ – $7h \ ^2H_{11/2}$	192.56		
$6h \ ^2H_{9/2}$ – $7i \ ^2I_{11/2}$	193.11		
$6h \ ^2H_{11/2}$ – $7i \ ^2I_{11/2}$	193.13		193.10 ± 0.02
$6h \ ^2H_{11/2}$ – $7i \ ^2I_{13/2}$	193.12		

Table 2. Experimental and theoretical fine-structure splittings $\Delta\nu(n\ell^2L)$ in cm^{-1} of the $5p(^2P)$, $5d(^2D)$, $8d(^2D)$ and $9p(^2P)$ terms of Ar VIII . (1) HFR calculations; (2) experimental data from Boduch *et al* (1992); (3) this experiment.

Fine structures	(1)	(2)	(3)
$\Delta\nu(5p\ ^2P)^a$	450.6	480 ± 5	482.8 ± 5.1
$^b$		485 ± 7	484.6 ± 8.6
$\Delta\nu(9p\ ^2P)^c$	70.1		77.2 ± 8.0
$^d$			74.6 ± 2.8
$\Delta\nu(5d\ ^2D)^b$	53.0	42 ± 7	41.3 ± 8.5
$\Delta\nu(8d\ ^2D)^d$	13.0		10.6 ± 2.8

^a From 5s–5p.^b From 5p–5d.^c From 8s–9p.^d From 8d–9p.**Table 3.** CTMC calculated emission cross sections (10^{-16} cm^2) versus the projectile energy (keV amu^{-1}) for single-electron capture following $\text{Ar}^{8+}\text{-Li}$ collisions.

Transition	Energy				
	0.1	0.2	0.5	0.8	1.0
5s–5p	0.176	0.156	0.131	0.113	0.106
5p–5d	0.930	0.837	0.692	0.574	0.524
6f–7g	2.95	3.17	3.92	4.50	4.77
6g–7h	12.06	15.32	21.20	25.38	27.38
6h–7i	36.30	62.39	82.81	103.68	112.63

for these wavelengths ($\lambda < 200 \text{ nm}$). However, the evolution of the intensities of these lines with the energy confirms the identifications; indeed, the intensities decrease with decreasing energies. Moreover, the calculated CTMC emission cross sections of lines corresponding to 5s–5p, 5p–5d, 6g–7h and 6h–7i transitions are presented in table 3 and will be discussed later on. These results corroborate the experimental identifications.

3. Single-electron capture cross sections

Experimental results

The experimental emission cross sections of all the observed lines are given in table 4 for projectile energies between 0.1 and 1.0 keV amu^{-1} . If a group of lines was not sufficiently resolved, the individual emission cross sections were deduced from the emission cross sections of the unresolved structure and from relative intensity measurements performed with narrower spectrometer slits. We have assumed that the relative uncertainties are always lower than $\pm 30\%$. The uncertainties of the experimental emission cross sections are due to the calibration method and the polarization effects. As the Ar^{8+} ion beam and the lithium jet are stable, the uncertainties due to the calibration depend mainly on the uncertainties of the cross sections for 1.5 keV amu^{-1} $\text{Ar}^{8+}\text{-Li}$ collisions. The uncertainties due to polarization effects are difficult to evaluate, but we can assume that the polarization rates are of the same order in this energy range. We assume that an upper limit of $\pm 30\%$

Table 4. Experimental emission cross sections (10^{-16} cm^{-2}) versus the projectile energy (keV amu^{-1}) for single-electron capture following Ar^{8+} -Li collisions. The experimental uncertainties are always lower than $\pm 30\%$.

Transition	Energy				
	0.1	0.2	0.5	0.8	1.0
5s-5p	0.29	0.18	—	—	—
5p-5d	1.04	0.61	—	—	—
7p-8s	1.35	3.30	3.83	5.58	4.47
7d-8p	6.13	7.89	5.86	3.95	2.56
7d-8f	2.05	0.89	0.33	0.30	0.24
7f-8d	1.18	1.04	0.39	0.43	0.33
7f-8g	6.07	3.01	2.05	2.05	1.55
7g-8h	17.26	12.27	9.80	8.94	7.79
7h-8i	32.93	42.16	36.81	36.90	32.82
7i-8k	59.38	108.71	90.55	99.83	88.80
8s-9p	1.00	0.67	0.30	0.23	*
8p-9s	19.92	15.82	8.71	5.47	2.83
8d-9p	5.84	3.69	1.22	1.15	1.24
8d-9f	0.34	0.27	0.20	0.13	0.14
8f-9d	0.46	0.43	0.13	0.11	0.08
8f-9g	0.95	0.94	0.87	0.92	0.69
8g-9h	1.99	2.54	2.94	4.03	3.31
8h-9i	5.89	6.51	9.68	11.21	9.39
8i-9k	10.62	10.59	15.93	21.28	19.38
8k-9l	11.30	15.72	18.29	33.84	30.01
8g-10h	0.06	0.07	0.16	0.33	0.26
8h-10i	0.07	0.08	0.23	0.38	0.34
8i-10k	0.08	0.10	0.26	0.47	0.45
8k-10l	0.12	0.07	0.24	0.57	0.51
9h-10i	0.18	0.09	0.32	0.66	0.74
9i-10k	0.25	0.12	0.42	0.96	1.14
9k-10l	0.64	0.15	0.68	1.98	2.17
9l-10m	0.48	0.14	0.48	3.43	2.34
9h-11i	0.01	0.02	0.06	0.22	0.35
9i-11k	0.01	0.03	0.11	0.36	0.56
9k-11l	0.02	0.02	0.08	0.27	0.42
9l-11m	0.01	0.01	0.04	0.12	0.18

for the relative uncertainties is large enough to take into account the most important error sources.

The $\sigma(n\ell)$ cross sections for single-electron capture into the 8ℓ and 9ℓ sublevels (i.e. for the most populated $n = 8$ and 9 states) were deduced from emission cross sections and transition probabilities. We used transition probabilities given by Lindgård and Nielsen (1977) for states with angular momenta $\ell \leq 4$ and hydrogenic transition probabilities for states with angular momenta $\ell \geq 5$. Lindgård and Nielsen do not give systematic errors for their calculations, but the transition probabilities obtained from HFR calculations differ by less than 5%. The experimentally determined $\sigma(n\ell)$ cross sections are then presented in table 5. For each $\sigma(n\ell)$ cross section, the uncertainty was deduced from the uncertainties

Table 5. Experimental cross sections (10^{-16} cm^2) versus the projectile energy (keV amu^{-1}) for single-electron capture into the 8ℓ and 9ℓ sublevels for Ar^{8+} -Li collisions.

$n\ell$	Energy				
	0.1	0.2	0.5	0.8	1.0
8s	11.5 ± 4.0	29.9 ± 9.4	35.2 ± 10.7	51.5 ± 15.6	41.4 ± 12.4
8p	53.9 ± 31.6	82.0 ± 36.9	64.9 ± 26.2	44.2 ± 17.5	29.5 ± 11.1
8d	41.1 ± 16.0	37.6 ± 13.7	14.3 ± 5.1	15.9 ± 5.5	11.7 ± 4.3
8f	54.0 ± 17.0	22.7 ± 7.6	8.0 ± 3.0	7.1 ± 2.8	5.7 ± 2.2
8g	39.8 ± 13.2	18.1 ± 7.0	11.1 ± 5.2	9.8 ± 5.6	7.1 ± 4.3
8h	52.1 ± 19.2	34.6 ± 14.3	23.5 ± 12.8	19.2 ± 12.5	17.1 ± 10.8
8i	47.8 ± 20.8	64.2 ± 25.7	49.2 ± 24.5	43.8 ± 26.2	38.5 ± 23.4
8k	48.0 ± 21.2	92.9 ± 37.3	72.0 ± 32.7	65.4 ± 40.3	58.3 ± 35.8
Total $n = 8$	349.1 ± 143.1	382.1 ± 151.9	278.1 ± 120.3	256.9 ± 125.8	209.3 ± 104.2
9s	246.0 ± 73.8	195.4 ± 58.6	107.5 ± 32.3	67.5 ± 20.3	34.9 ± 10.5
9p	105.4 ± 31.6	69.0 ± 20.7	27.7 ± 8.3	22.8 ± 6.8	20.6 ± 6.2
9d	21.9 ± 6.6	20.3 ± 6.1	6.4 ± 1.9	5.3 ± 1.6	3.7 ± 1.1
9f	14.3 ± 4.3	11.3 ± 3.4	8.2 ± 2.5	5.4 ± 1.6	6.0 ± 1.8
9g	10.0 ± 3.0	9.9 ± 3.0	9.1 ± 2.7	9.7 ± 2.9	7.3 ± 2.2
9h	10.2 ± 3.2	13.2 ± 4.0	15.0 ± 4.7	20.2 ± 6.6	16.2 ± 5.5
9i	16.9 ± 5.2	18.8 ± 5.7	27.7 ± 8.6	31.4 ± 10.2	25.7 ± 8.7
9k	16.9 ± 5.4	17.3 ± 5.3	25.5 ± 8.1	32.9 ± 11.2	29.4 ± 10.3
9l	10.8 ± 3.5	15.6 ± 4.8	17.8 ± 5.6	30.3 ± 11.1	27.5 ± 9.7
Total $n = 9$	431.4 ± 130.3	352.7 ± 106.2	229.0 ± 70.0	206.5 ± 66.6	152.0 ± 50.2

of the emission cross sections. For example,

$$\sigma(8p) = \frac{\sigma_{\text{em}}(7d-8p)}{0.077} - \sigma_{\text{em}}(8p-9s)$$

and

$$\Delta\sigma(8p) = \frac{\Delta\sigma_{\text{em}}(7d-8p)}{0.077} + \Delta\sigma_{\text{em}}(8p-9s).$$

The relative uncertainties are then between $\pm 30\%$ and $\pm 65\%$ ($\Delta\sigma(8h)$ for $0.8 \text{ keV } \text{amu}^{-1}$).

CTMC calculated cross sections

Cross sections for capture into the different $n\ell$ sublevels were calculated by using the three-body CTMC method. In the classical approach, the Hamilton equations for the motion of three classical particles, i.e. the valence electron and its parent core Li^+ plus the ionic core projectile Ar^{8+} , are solved for a given set of initial conditions for the projectile and the target (each set of initial condition defines a classical trajectory). Details on the CTMC method which uses effective electron-core interactions and the method of Reinhold and Falcon (1986) for the initialization of the target electron are given by Pascale *et al* (1990). In the present study of $\text{Ar}^{8+} + \text{Li}(2s)$ collisions, local model potentials were used to describe the effective interactions between the electron and the two closed-shell ionic cores (see Jacquet *et al* 1995). The binning procedure of the classical quantities (binding energy and angular momentum of the captured electron) to determine the final $n\ell$ sublevels, and which takes into account the asymptotic quantum defects of the Ar^{7+} energy levels (Theodosiou *et al* 1986), has been described previously (Jacquet *et al* 1995). The calculations were performed with a sufficiently large number of trajectories (between 7.5×10^3 and 1.25×10^4 trajectories)

to ensure statistical errors of less than 3% for the most populated 8ℓ and 9ℓ sublevels. For the smallest cross sections of the 8ℓ - and 9ℓ -distributions, the statistical errors never exceed 6%. In the figures, the symbols representing the CTMC calculated values are mostly larger than the statistical error bars which therefore have not been drawn.

The calculated final $n\ell$ -distributions ($n = 8$ and 9) are reported in table 6 for the Ar^{8+} -Li(2s) collisions, at all the projectile energy values investigated experimentally. Moreover, and in order to clearly show the effect of the Ar^{8+} -core electrons on the $n\ell$ -distributions (see the discussion in section 3), the CTMC calculated 8ℓ - and 9ℓ -cross sections for the O^{8+} -Li(2s) collisions are also given in table 6 at some energies (0.1, 0.5 and 1 keV amu^{-1}). The corresponding CTMC calculated emission cross sections of the experimentally observed lines in Ar^{8+} -Li(2s) collisions are then given in tables 3 and 7 for comparison with the measured emission cross sections (see table 5). On the whole, the agreement between the CTMC calculated and measured emission cross sections is fair concerning the behaviour of the cross sections with the projectile energy. An exception has to be made for the lines corresponding to the $7\ell'-8\ell$ transitions ($\ell \geq 5$) where the calculated emission cross sections decrease with decreasing energies when, correspondingly, the measured cross sections increase (7g–8h) or are almost constant within the error bars (7h–8i and 7i–8k). Some of the calculated emission cross sections increase (or decrease) more or less fast with decreasing energies than do the experimental ones (7p–8s, 7f–8g, 8p–9s, 8i–9k and 8k–9l transitions). As regards the absolute values, some of the CTMC calculated emission cross sections are well outside the estimated experimental uncertainties. In particular, some discrepancies are observed for the lines corresponding to the $8p$ – $9s$ and $7\ell'-8\ell$ ($\ell \geq 4$) transitions at energies smaller than 0.2 keV amu^{-1} . Similar

Table 6. CTMC calculated cross sections (10^{-16} cm^2) versus the projectile energy (keV amu^{-1}) for single-electron capture into the 8ℓ and 9ℓ sublevels for X^{8+} -Li collisions. (1) $\text{X} \equiv \text{O}$ and (2) $\text{X} \equiv \text{Ar}$.

$n\ell$	Energy							
	0.1		0.2	0.5		0.8	1.0	
	(1)	(2)	(2)	(1)	(2)	(2)	(1)	(2)
8s	7.7	18.8	23.3	2.3	27.6	29.3	2.1	28.2
8p	20.1	75.0	82.1	7.0	83.4	69.9	5.8	61.3
8d	33.0	79.7	55.8	12.2	32.5	24.3	9.9	19.8
8f	39.2	41.8	26.2	20.0	14.7	10.7	16.6	9.3
8g	40.9	20.1	17.5	28.0	14.5	13.5	25.5	13.3
8h	41.2	19.5	21.4	37.7	21.1	21.9	35.1	21.3
8i	33.1	24.8	31.0	52.2	34.1	35.2	47.6	34.6
8k	20.9	23.7	42.9	71.3	49.1	51.2	67.0	52.8
Total $n = 8$	236.0	303.4	300.2	230.8	277.0	256.0	209.6	240.4
9s	4.8	61.9	55.8	2.2	46.2	37.7	1.9	33.8
9p	15.9	109.7	91.6	8.0	58.4	37.6	5.4	29.7
9d	27.8	46.2	33.2	14.4	18.5	14.0	10.0	12.4
9f	42.8	14.3	14.8	21.1	9.3	7.0	14.9	6.6
9g	51.6	7.8	10.0	28.8	10.7	12.2	21.2	10.5
9h	51.1	7.9	9.7	37.9	15.7	18.9	31.1	19.3
9i	38.3	9.5	12.0	43.9	21.5	27.9	42.7	29.7
9k	19.1	10.7	11.8	42.9	21.8	32.2	48.4	36.6
9l	6.5	4.9	8.4	22.6	11.7	22.4	38.0	26.1
Total $n = 9$	257.9	272.9	247.3	221.2	213.8	209.9	213.6	204.6

Table 7. CTMC calculated emission cross sections (10^{-16} cm^2) versus the projectile energy (keV amu^{-1}) for single-electron capture following Ar^{8+} -Li collisions.

Transition	Energy				
	0.1	0.2	0.5	0.8	1.0
7p-8s	2.16	2.53	3.08	3.22	3.10
7d-8p	6.27	6.73	7.55	5.67	4.98
7d-8f	1.59	1.02	0.598	0.452	0.399
7f-8d	2.13	1.52	0.893	0.665	0.539
7f-8g	3.15	2.85	2.60	2.58	2.61
7g-8h	6.89	7.76	8.82	9.82	10.06
7h-8i	17.69	21.89	27.54	32.21	34.01
7i-8k	29.19	51.80	62.08	77.39	82.60
8s-9p	1.01	0.843	0.538	0.347	0.275
8p-9s	5.02	4.52	3.74	3.05	2.74
8d-9p	6.61	5.52	3.52	2.27	1.80
8d-9f	0.341	0.353	0.225	0.170	0.161
8f-9d	0.974	0.700	0.392	0.297	0.264
8f-9g	0.749	0.966	1.05	1.19	1.05
8g-9h	1.54	1.90	3.10	3.75	3.92
8h-9i	3.36	4.25	7.69	10.04	10.90
8i-9k	6.42	7.43	13.88	20.73	23.84
8k-9l	5.19	8.65	12.37	25.01	28.22
8g-10h	0.106	0.165	0.313	0.466	0.613
8h-10i	0.152	0.247	0.620	0.751	1.08
8i-10k	0.197	0.333	0.771	1.05	1.59
8k-10l	0.230	0.197	0.560	1.03	1.43
9h-10i	0.128	0.207	0.520	0.630	0.905
9i-10k	0.210	0.354	0.818	1.12	1.69
9k-10l	0.409	0.351	0.997	1.83	2.53
9l-10m	0.243	0.259	0.624	2.49	2.01
9h-11i	0.013	0.022	0.061	0.107	0.269
9i-11k	0.028	0.039	0.090	0.164	0.342
9k-11l	0.019	0.028	0.067	0.128	0.250
9l-11m	0.020	0.025	0.034	0.120	0.111

differences are also found for the lines corresponding to the $8f-9d$ and $8\ell'-10\ell$ ($\ell \geq 5$) transitions where the calculated values are a factor of 2–4 larger than the experimental ones over the entire energy range.

The CTMC calculated emission cross sections reported in table 3 for the Ar^{8+} -Li(2s) collisions are mainly due to cascades from the most populated $n = 8$ and 9 levels. More specifically, we have verified that the emission cross sections corresponding to the $5s-5p$ and $5p-5d$ transitions are due to cascades from the 8ℓ and 9ℓ sublevels with $\ell \leq 3$ and those corresponding to the $6f-7g$, $6g-7h$ and $6h-7i$ transitions are due to cascades from the 8ℓ and 9ℓ sublevels with $\ell \geq 4$. Therefore, the energy dependence of these emission cross sections is closely connected with the energy dependence of the cross sections for electron capture into the 8ℓ and 9ℓ sublevels (see tables 3 and 7).

Before we discuss the results obtained for the $n\ell$ cross sections, let us consider the cross sections $\sigma(n)$ for electron capture into specific n levels, as well as the total electron capture cross section $\sigma_t = \sum_n \sigma(n)$. In table 8 we report the results obtained in the range 0.1–1 keV amu^{-1} for the CTMC calculated cross sections $\sigma(n)$ and σ_t for O^{8+} -Li(2s)

Table 8. CTMC calculated cross sections (10^{-16} cm²) for single-electron capture into n levels in O^{8+} -Li(2s) and Ar^{8+} -Li(2s) collisions, versus the projectile energy (keV amu⁻¹). The total single-electron capture cross section is also reported.

n	Energy							
	0.1	0.2	0.5	0.8	1.0	2.0	3.0	4.0
O^{8+}								
6	1.1		1.7		3.2	6.0	5.7	6.3
7	13.6		33.7		39.5	41.8	43.1	43.4
8	236.0		230.8		209.6	183.5	166.1	160.9
9	257.8		221.9		213.6	226.1	219.9	222.8
10	17.1		30.1		40.9	47.1	53.5	52.2
11	1.6		5.7		12.7	8.3	15.5	10.5
12	0.1		1.5		3.7	3.1	5.2	4.0
Total	527.4		526.7		524.9	522.2	517.7	506.5
Ar^{8+}								
6	0.3	0.5	1.6	2.1	3.5	6.8	6.6	5.8
7	20.2	26.8	41.1	44.7	48.7	48.9	46.1	44.0
8	303.3	299.3	277.0	256.1	240.4	193.1	164.8	156.6
9	272.5	247.4	213.8	209.8	204.6	210.4	214.4	217.5
10	13.1	14.9	19.7	230.1	27.5	40.8	50.7	50.8
11	1.5	1.6	3.4	4.3	7.4	7.8	14.3	12.5
12	0.5	0.5	0.7	1.3	2.3	2.3	4.9	5.2
Total	612.8	592.3	558.4	543.3	536.3	515.9	509.6	502.1

and Ar^{8+} -Li(2s) collisions, along with previous results (Jacquet *et al* 1995, Jacquet and Pascale 1995) obtained in the range 1–4 keV amu⁻¹. As seen in the table, the energy dependence of the n -distributions is similar for O^{8+} and Ar^{8+} . The n -distributions are mainly peaked on $n = 8$ and 9, but they broaden towards lower and higher n levels at the highest energies. However, some differences in the behaviour of the $n = 8$ and 9 cross sections with the projectile energy have to be noted. For the two projectiles, the $n = 8$ cross section increases continuously with decreasing energies, with a stronger variation for Ar^{8+} than for O^{8+} . In contrast, the energy dependence of the $n = 9$ cross section is nearly the same over all the energy range for the two projectiles: the cross section is nearly constant in the range 0.5–4 keV amu⁻¹ and then increases below 0.5 keV amu⁻¹, where in the case of Ar^{8+} , the variation is stronger for $n = 9$ than for $n = 8$. As is discussed later on, these differences in the behaviour of the $n = 8$ and 9 cross sections may be explained by the competition between the projectile-core-electron effect and the Stark effect, and by different contributions with the projectile energy of the non-adiabatic couplings involved in the electron capture process. In particular, at the highest energies where the Stark effect dominates, the $\sigma(n)$ cross sections tend to be the same for O^{8+} and Ar^{8+} (see table 8).

Figures 2(a) and (b) show the CTMC calculated cross sections $\sigma(n)$ for $n = 8$ and 9 compared with the experimental ones for Ar^{8+} -Li(2s) collisions, in the range 0.1–4.5 keV amu⁻¹. The experimental results obtained at higher energy, i.e. in the range 1.5–4.5 keV amu⁻¹, have already been presented by Jacquet *et al* (1995). However, some modifications have to be noted concerning these results. Indeed, in this energy range, the calibration used for the determination of the experimental cross sections was revised and the experimental cross sections reported here are slightly different from those published previously. However, these corrections do not induce important modifications in the cross sections. As can be seen in figure 2(a), the CTMC calculated cross sections for

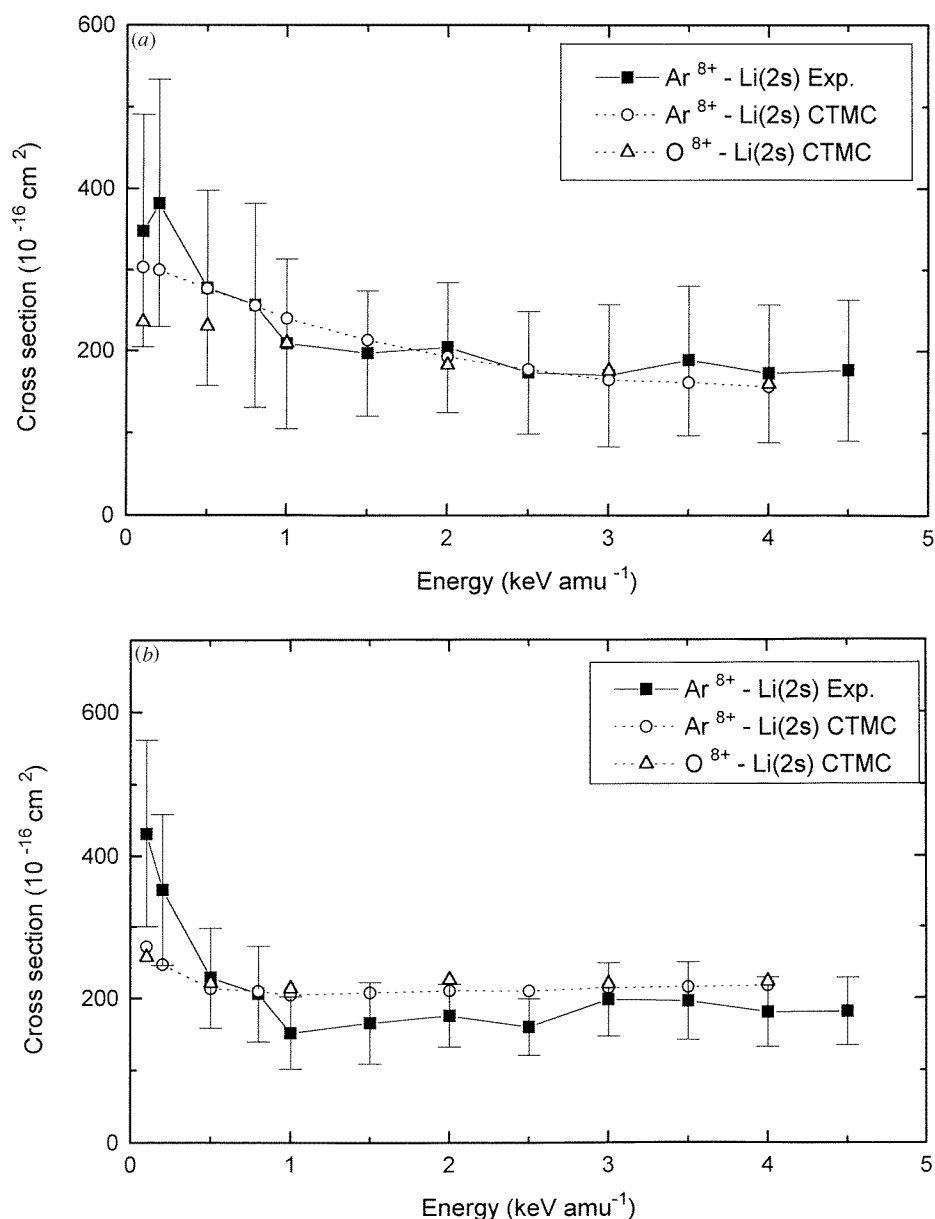


Figure 2. Experimental and CTMC calculated $\sigma(n)$ total cross sections (10^{-16} cm^2) for O^{8+} and Ar^{8+} -Li(2s) collisions versus projectile energy (keV amu^{-1}). The curves have been drawn to help guide the eye. (a) $n = 8$; (b) $n = 9$.

electron capture into the $n = 8$ levels are in fair agreement with the present experimental results. In figure 2(b), showing the population of the $n = 9$ shell, the experimental cross sections are larger than the CTMC calculated ones, for projectile energies of 0.1 and 0.2 keV amu^{-1} . These differences result from large discrepancies between experimental and CTMC calculated $\sigma(9s)$ and $\sigma(9p)$ cross sections (see tables 6 and 7).

The cross section σ_t for total electron capture in O^{8+} -Li(2s) collisions is almost constant in the energy range 0.1–4 keV amu⁻¹ (see table 8). This result is in agreement with the scaling formula of Schweinzer *et al* (1994). They predict a constant value of 9.0×10^{-16} cm² for a total reduced cross section over all the present energy range; our results for O^{8+} find an almost constant reduced cross section of 1.0×10^{-15} cm². In the case of Ar^{8+} -Li(2s) collisions, σ_t increases monotonically with decreasing energies, the corresponding total reduced cross section varying from 9.9×10^{-15} cm² at 4 keV amu⁻¹ to 1.2×10^{-15} cm² at 0.1 keV amu⁻¹. However, the σ_t cross section for Ar^{8+} varies little in the energy range 1–4 keV amu⁻¹ and agrees to within less than 2% with the one for O^{8+} . At energies below 1 keV amu⁻¹, the increasing difference (up to 16%) between the σ_t cross sections for O^{8+} and Ar^{8+} as the energy decreases can be attributed to the increasing effect of the Ar^{8+} core electrons. As discussed later on, in the case of Ar^{8+} -Li(2s) collisions, several primary radial couplings can contribute to the electron capture into each of the $n = 8$ and 9 levels, whereas only one primary radial coupling contributes to each of them for O^{8+} -Li(2s) collisions.

4. $n\ell$ distributions and charge exchange process

The $n\ell$ distributions result from both the primary capture process and the post-collisional effects: these two processes depend on the relative importance of the radial and rotational couplings and on the Stark mixing and the projectile-core-electron effect. In the case of fully stripped ions colliding with lithium atoms (O^{8+} -Li), all $n\ell$ sublevels (n fixed) are affected by the Stark effect due to the Li^+ residual ion. The population of states with large ℓ values is then favoured and then only states with large ℓ values are populated by single-electron capture. In the case of Ar^{8+} -Li collisions, the presence of the projectile core electrons lifts the degeneracy of the $Ar^{7+}(n\ell)$ states with low ℓ values ($\ell < 4$) and only the states with high ℓ values are affected by the Stark effect. We have already shown that the $\sigma(n\ell)$ cross sections for $\ell < 4$ are strongly affected by the core-electron effect at low energy (Jacquet *et al* 1995). It leads to the enhancement of the population of states with low ℓ values. The evolution of the $n\ell$ distributions with the projectile velocity depends on the evolution of the dynamical couplings. Indeed, in the 1.5–4.5 keV amu⁻¹ energy range, we have shown that the effect of the projectile core electrons vanishes at high energies (Jacquet *et al* 1995, Jacquet and Pascale 1995) and increases as the projectile energy decreases.

Harel and Jouin (1988) have made an extensive study of single-electron capture in X^{8+} -H(1s) collisions ($X \equiv O, Ne, Ar$) for the 1–16 keV amu⁻¹ energy range by using a semiclassical close-coupling method with a molecular expansion of one-electron diatomic molecule (OEDM) orbitals including translation factors. For these collisions, where the most populated level is $n = 5$, they have shown the influence of the projectile-core electrons on the 5ℓ -distribution. In particular, they have found that the core-electron effect vanishes at large energies, the population of the $n\ell$ -sublevels being dominated by the Stark effect of the residual ion. The Ar^{8+} -Li(2s) system seems to be more appropriate for studying the competition between the Stark effect and the core-electron effect for populating the $n\ell$ -sublevels as a function of the energy. Indeed, for this collision system, the most populated levels are $n = 8$ and 9, and therefore many states with large values of ℓ are available. However, for this system, close-coupling calculations similar to those performed by Harel and Jouin (1988) seem to be difficult to achieve in view of the large number of molecular channels which would be required.

In a previous work (Laulhé *et al* 1997), we have presented calculations of the electronic energies of a one-electron $(X^{7+} + Li)^+$ system ($X \equiv O$ and Ar) made by using a pseudo-

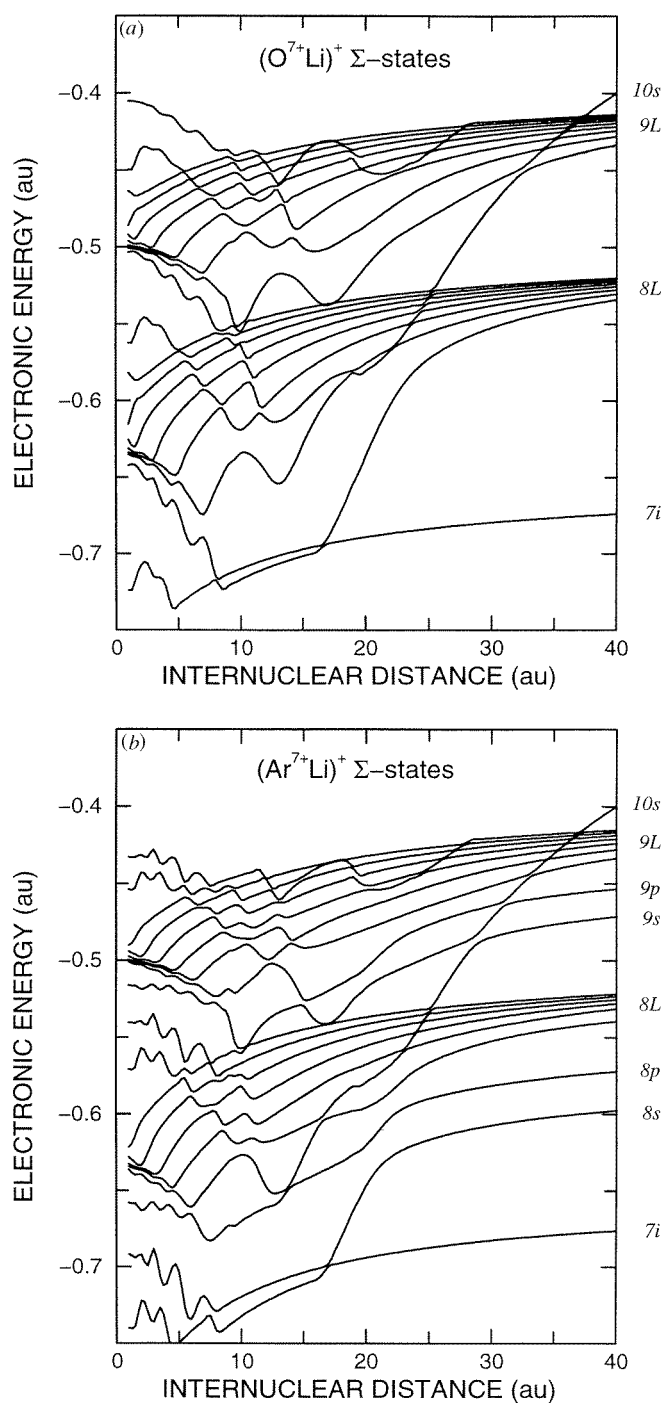


Figure 3. Calculated electronic energy (au) versus the internuclear distance (au) for $(\text{X}^{7+}\text{Li})^+$ Σ -states. (a) $\text{X} \equiv \text{O}$; (b) $\text{X} \equiv \text{Ar}$.

potential method. The electronic energies were calculated for each symmetry Λ of the system, where Λ is the absolute value of the projection of the total orbital momentum of the system along the internuclear axis (taken as the quantization axis). These calculations allow us to discuss the calculated CTMC results and the experimental ones in terms of dynamical couplings: radial couplings between molecular states with $\Delta\Lambda = 0$ and rotational couplings for $\Delta\Lambda = \pm 1$. For the internuclear distance range $R = 1\text{--}40$ au, the electronic energies relevant to the capture into the levels $n = 8$ and 9 of X^{7+} are shown for the Σ symmetry in figures 3(a) and (b). The two electronic energy curves just above and just below the two manifolds of energy curves are also shown in the figures. In particular, the Σ -energy curve just above the manifold correlating to the $n = 9$ level of the X^{7+} ion is the entrance channel for the electron capture process. This Σ -energy curve goes to the $2s$ state of Li at large R values through numerous diabatic crossings of the Σ -energy curves.

If we consider the $(O^{7+} + Li)^+$ system, there are two avoided crossings between the entrance channel and the lowest Σ -energy curves correlating, respectively, to the $n = 8$ and 9 levels ($R \approx 22.5$ au for $n = 8$ and $R \approx 32.4$ au for $n = 9$). These avoided crossings are responsible for the primary radial couplings ($\Delta\Lambda = 0$) leading to electron capture into the $n = 8$ and 9 levels. Then the 8ℓ and 9ℓ states are populated by the Stark effect of the residual Li^+ ion at large R values. More precisely, successive rotational couplings between molecular states with $\Delta\Lambda = \pm 1$ lead to large values of ℓ due to the degeneracy of the 8ℓ and 9ℓ sublevels in O^{7+} . But since the rotational couplings are less efficient at low energy, the population of the highest ℓ -values should decrease progressively with decreasing energies, and at the benefit of the low ℓ -values below. This is observed in the CTMC calculated 8ℓ - and 9ℓ -distributions (table 6). Moreover, the avoided crossings mentioned above show different energy splittings (see figure 3(a)). In particular, the primary radial coupling responsible for populating the 9ℓ -states should be more efficient at very low energy than the one populating the 8ℓ -states. Consequently, the decrease of the population

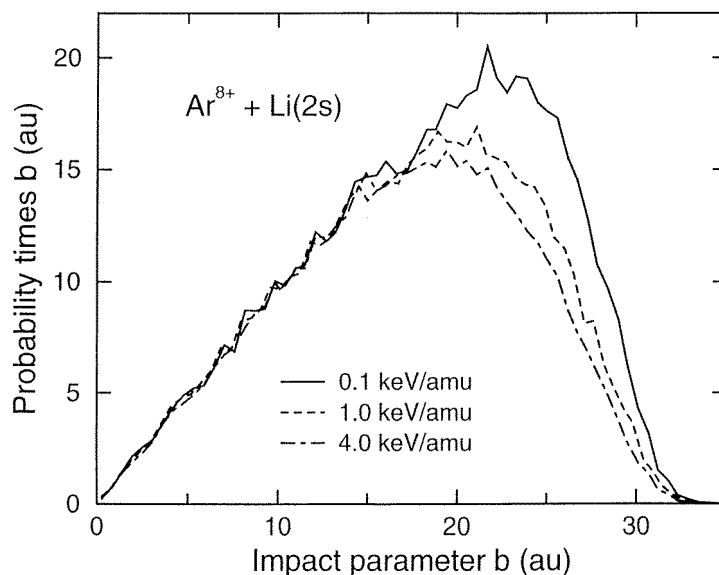


Figure 4. CTMC calculated probability times b versus impact parameter b for $Ar^{8+}\text{--}Li(2s)$ collisions for projectile energies $E = 0.1, 1.0$ and 4.0 keV amu^{-1} .

of large ℓ values, at the benefit of low ℓ values, should be more visible for the 9ℓ -distribution than for the 8ℓ -distribution. This is found in our CTMC calculations (table 6).

If we consider the $(\text{Ar}^{7+} + \text{Li})^+$ system, the degeneracy of the levels for $\ell \leq 2$ is removed by the core electrons in the separated-atom limit. It results that the Σ -electronic energy curves correlating to these levels show up avoided crossings with the entrance channel in the region $R \approx 20$ –23 au for those correlating to the 8s, 8p and 8d states and $R \approx 28$ –33 au for those correlating to the 9s, 9p and 9d states. These avoided crossings are responsible for the primary radial couplings leading to the electron capture into the $n = 8$ and 9 levels. Note that the regions of radial couplings are consistent with the maximum value of the impact parameters b which contribute significantly to the CTMC calculated cross sections, that is $b_{\text{max}} \approx 35$ au (see figure 4). Because the 8ℓ and 9ℓ states ($\ell \leq 2$) are non-degenerate, the rotational couplings at large R values between the molecular states correlating to these states are less efficient for Ar^{8+} -Li collisions than for O^{8+} -Li collisions. The core-electron effect is then responsible for the population of states with low ℓ values as it is experimentally observed and theoretically calculated by using the CTMC method (tables 5 and 6).

We have already shown that at high energies, the $n\ell$ distributions are not affected by the projectile core-electron effect (Jacquet *et al* 1995, Jacquet and Pascale 1995). In that case, and as for O^{8+} -Li(2s) collisions, only the states with large ℓ -values are populated by the Stark effect in Ar^{8+} -Li(2s) collisions. This can be observed in figure 5(a) which shows the experimental and CTMC 8ℓ -distributions at an energy of 4.0 keV amu^{-1} . As the energy decreases, the radial couplings at the avoided crossings between the Σ -molecular states become more and more efficient, whereas the intershell rotational couplings decrease, beginning with those associated with the lowest $\text{Ar}^{7+}(n\ell) + \text{Li}^+$ outgoing channels. Therefore, at low energies, the 8ℓ -distribution for Ar^{8+} -Li(2s) collisions should be rather different from the one for O^{8+} -Li(2s) collisions. This can be seen in figure 5(b), where the experimental and CTMC calculated 8ℓ -distributions are shown at an energy of 0.5 keV amu^{-1} . As expected, the low ℓ -values of the 8ℓ -distribution for Ar^{8+} -Li(2s) collisions are significantly populated. However, the large ℓ -values are also almost as populated as for O^{8+} -Li(2s) collisions, indicating that at this energy, the Stark effect is still very efficient in Ar^{8+} -Li(2s) collisions. This can be explained as follows: as the energy decreases, the primary radial couplings associated with the 8p state and then the 8d state become successively more and more efficient, leading to population by successive rotational couplings of the large values of ℓ . Therefore, at much lower energies, and as explained previously for O^{8+} -Li(2s) collisions, the population of the highest ℓ -values should decrease at the benefit of the other ℓ -values. This is indeed observed in tables 5 and 6 where, as for O^{8+} -Li(2s) collisions, the effect is more visible for the 9ℓ -distribution than for the 8ℓ -distribution.

The energy splittings at the avoided crossings associated with the $n = 8$ levels are much larger than the ones associated with the $n = 9$ levels. Therefore, as the energy decreases, the core-electron effect in Ar^{8+} -Li(2s) collisions occurs first in the final 8ℓ distribution and at lower energies in the 9ℓ distributions. This is in agreement with the maximum in the CTMC calculated total probability time impact parameter, which shifts from $b \approx 20$ au at impact energies $E > 1$ keV amu^{-1} to $b \approx 23$ au at an impact energy of $E \approx 0.1$ keV amu^{-1} , while the maximum value increases slightly with decreasing energies (cf figure 4). Because of different energy splittings at the avoided crossings, all the cross sections for capture into $n\ell$ sublevels with $\ell \leq 2$ should go through a maximum as the energy decreases, beginning with those associated with the largest energy splittings. Within the same n -level, this should occur successively for capture into the s-sublevel, then for the p-sublevel and finally for the d-sublevel, in the assumption of direct coupling between the

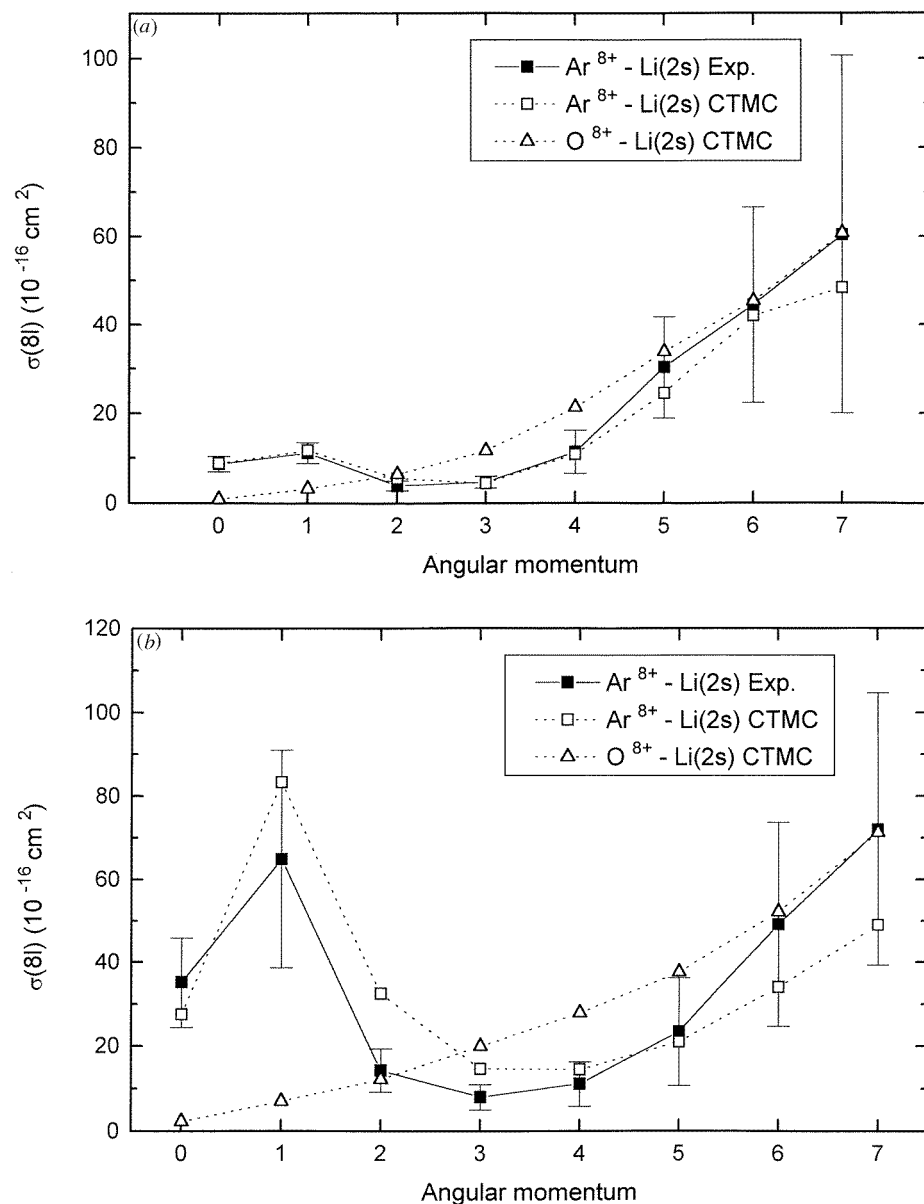


Figure 5. 8ℓ -distributions (10^{-16} cm^2) for $\text{X}^{8+} - \text{Li}(2s)$ collisions. For $\text{X} \equiv \text{Ar}$, experimental and CTMC calculated cross sections are shown and for $\text{X} \equiv \text{O}$, CTMC calculated cross sections are shown. The lines have been drawn to help guide the eye. (a) Projectile energy of 4.0 keV amu⁻¹; (b) projectile energy of 0.5 keV amu⁻¹.

entrance channel and the various capture channels. Indeed, both in the experimental results and in the CTMC calculated ones, $\sigma(8s)$ goes through a broad and shallow maximum for a projectile energy of about 0.8 keV amu⁻¹ (cf figure 6(a)). It can also be seen that the CTMC calculated $\sigma(8p)$ cross section goes through a maximum between 0.2 and 0.5 keV amu⁻¹ (cf figure 6(b)) which is not clearly seen in the experimental cross section

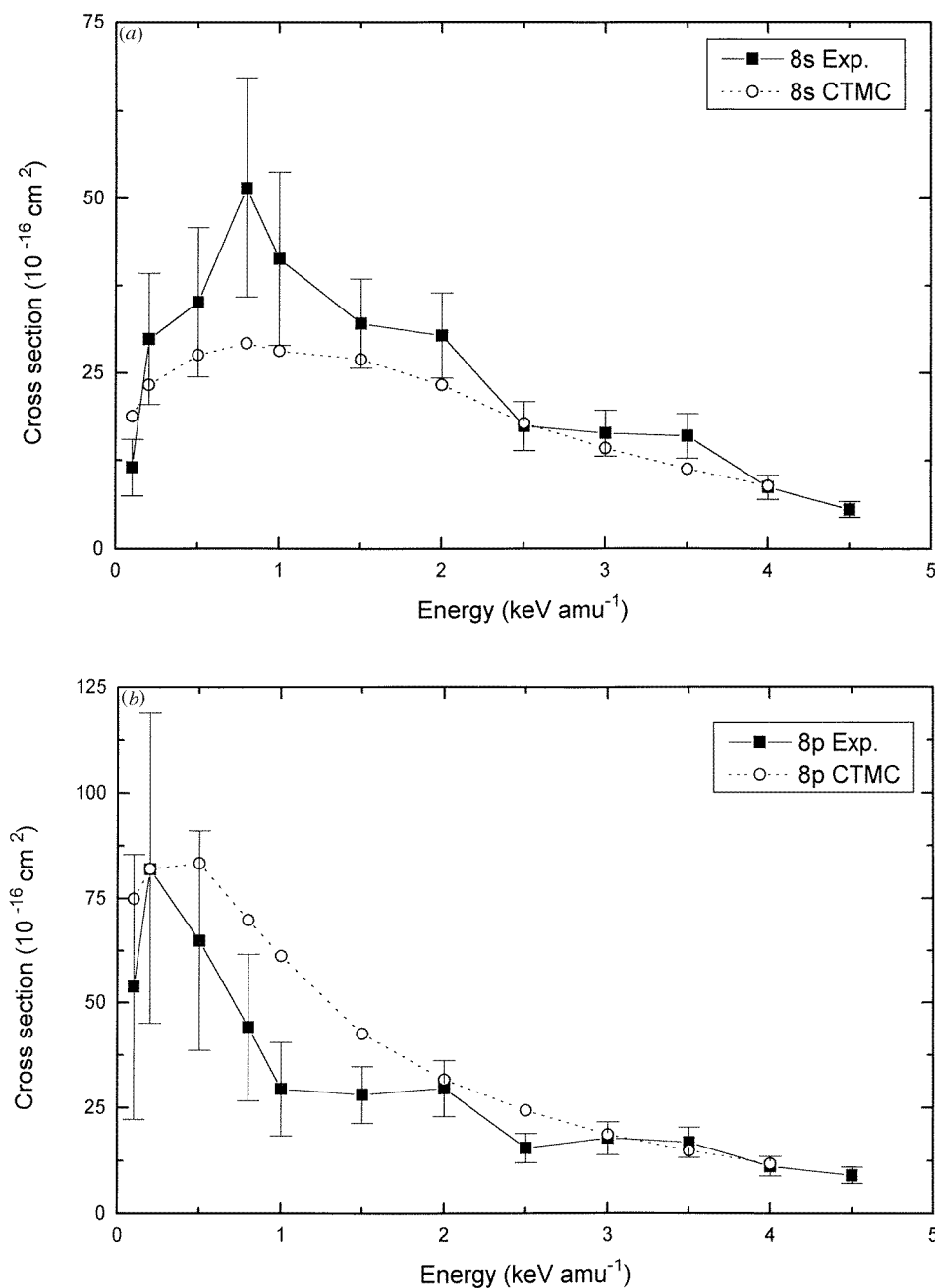


Figure 6. Experimental and CTMC calculated 8ℓ cross sections (10^{-16} cm^2) for Ar^{8+} -Li(2s) collisions versus the collision energy (keV amu^{-1}). The lines have been drawn to help guide the eye. (a) $\ell = 0$; (b) $\ell = 1$.

due to large uncertainties. No maximum is observed for $\sigma(8d)$, $\sigma(9s)$, $\sigma(9p)$ and $\sigma(9d)$ cross sections.

The experimental and CTMC calculated $\sigma(9s)$ and $\sigma(9p)$ cross sections show up large discrepancies (see tables 5 and 6) especially for the projectile energies of 0.1 and 0.2 keV amu⁻¹, which are not explained at present. The CTMC method does not seem to have reached its low-energy limit of validity in view of the fair agreement between the experimental results and all the other CTMC calculated $n\ell$ cross sections.

5. Conclusion

Collisions between Ar⁸⁺ ions and Li atoms have been studied experimentally for incident energies from 0.1 to 1.0 keV amu⁻¹ and studied theoretically by using the CTMC method. We have shown that, in addition to the effect of the projectile core electrons, the $n\ell$ cross sections depend strongly on the velocity of the incident ions. Both the experimental and the CTMC calculated results have been analysed in terms of dynamical couplings by using calculations of the electronic energies of one-electron (X⁷⁺-Li)⁺ systems (X \equiv O, Ar). At low energies, the radial couplings at the avoided crossings between the entrance channel and the Ar⁷⁺($n\ell$) + Li⁺ outgoing channels ($n = 8$ and 9 , $\ell = 0, 1, 2$) are efficient. As a result, the $\sigma(n\ell)$ cross sections increase with decreasing energy for a given $n\ell$ state ($n = 8, 9$ and $\ell = 0, 1, 2$) and should go through a maximum. Indeed, for $\sigma(8s)$, this maximum is seen in both experimental and CTMC calculated results.

References

- Abrines R and Percival I C 1966 *Proc. Phys. Soc.* **88** 861–72
- Boduch P, Chantepie M, Hennecart D, Husson X, Kucal H, Lecler D, Stolterfoht N, Druetta M, Fawcett B and Wilson M 1992 *Phys. Scr.* **45** 203–11
- Brazuk A, Winter H, Dijkkamp D, de Heer F J and Drentje A G 1985 *Nucl. Instrum. Methods B* **9** 442
- Cowan R D 1981 *The Theory of Atomic Structure and Spectra* (Berkeley, CA: University of California Press)
- Jacquet E and Pascale J 1995 *Nucl. Instrum. Methods B* **98** 253
- Jacquet E, Pascale J, Boduch P, Chantepie M and Lecler D 1995 *J. Phys. B: At. Mol. Opt. Phys.* **28** 2221
- Jacquet E *et al* 1993 *Phys. Scr.* **47** 618–27
- Jacquet E *et al* 1994 *Phys. Scr.* **49** 154–65
- Harel C and Jouin H 1988 *J. Phys. B: At. Mol. Opt. Phys.* **21** 859
- Hoekstra R, Olson R E, Folkerts H O, Wolfrum E, Pascale J, de Heer F J, Morgenstern R and Winter H 1993 *J. Phys. B: At. Mol. Opt. Phys.* **26** 2029
- Laulhé C, Jacquet E, Cremer G, Pascale J, Boduch P, Rieger G, Chantepie M and Lecler D 1997 *Phys. Rev. A* **55** 1088
- Lindgård A and Nielsen S E 1977 *At. Data Nucl. Data Tables* **19** 563
- Olson R E and Salop A 1977 *Phys. Rev. A* **16** 531
- Pascale J, Olson R E and Reinhold C O 1990 *Phys. Rev. A* **42** 5305
- Reinhold C O and Falcon C A 1986 *Phys. Rev. A* **33** 3859
- Rieger G, Boduch P, Chantepie M, Jacquet E, Lecler D and Pascale J 1995 *J. Phys. B: At. Mol. Opt. Phys.* **28** 2689
- Schorn R P, Hink E, Rusbüldt D, Schneider M, Unterreiter E and Winter H 1991 *Appl. Phys. B* **52** 71
- Schweitzer J, Wutte D and Winter H P 1994 *J. Phys. B: At. Mol. Opt. Phys.* **27** 137
- Theodosiou C E, Inokuti M and Manson S T 1986 *At. Data Nucl. Data Tables* **19** 473
- Wolfrum E, Hoekstra R, de Heer F J, Morgenstern R and Winter H 1992 *J. Phys. B: At. Mol. Opt. Phys.* **25** 2597